

Research Article

Micelle-Assisted Synthesis of $\text{Al}_2\text{O}_3\cdot\text{CaO}$ Nanocatalyst: Optical Properties and Their Applications in Photodegradation of 2,4,6-Trinitrophenol

Ayesha Imtiaz,¹ Muhammad Akhyar Farrukh,¹
Muhammad Khaleeq-ur-rahman,¹ and Rohana Adnan²

¹ Department of Chemistry, GC University Lahore, 54000 Lahore, Pakistan

² School of Chemical Sciences, Universiti Sains Malaysia, 11800 Pulau Pinang, Malaysia

Correspondence should be addressed to Muhammad Akhyar Farrukh; akhyar100@gmail.com

Received 26 August 2013; Accepted 19 September 2013

Academic Editors: O. Gonzalez Diaz and J. Yu

Copyright © 2013 Ayesha Imtiaz et al. This is an open access article distributed under the Creative Commons Attribution License, which permits unrestricted use, distribution, and reproduction in any medium, provided the original work is properly cited.

Calcium oxide (CaO) nanoparticles are known to exhibit unique property due to their high adsorption capacity and good catalytic activity. In this work the CaO nanocatalysts were prepared by hydrothermal method using anionic surfactant, sodium dodecyl sulphate (SDS), as a templating agent. The as-synthesized nanocatalysts were further used as substrate for the synthesis of alumina doped calcium oxide ($\text{Al}_2\text{O}_3\cdot\text{CaO}$) nanocatalysts via deposition-precipitation method at the isoelectric point of CaO. The $\text{Al}_2\text{O}_3\cdot\text{CaO}$ nanocatalysts were characterized by FTIR, XRD, TGA, TEM, and FESEM techniques. The catalytic efficiencies of these nanocatalysts were studied for the photodegradation of 2,4,6-trinitrophenol (2,4,6-TNP), which is an industrial pollutant, spectrophotometrically. The effect of surfactant and temperature on size of nanocatalysts was also studied. The smallest particle size and highest percentage of degradation were observed at critical micelle concentration of the surfactant. The direct optical band gap of the $\text{Al}_2\text{O}_3\cdot\text{CaO}$ nanocatalyst was found as 3.3 eV.

1. Introduction

Metal oxide nanoparticles play effective role in degradation of hazardous chemicals. Their highly intrinsic surface area and catalytic properties have made them destructive adsorbents. These metal oxides not only adsorb hazardous chemicals on their surface but also destroy them into smaller and less harmful by-products [1, 2]. They can destroy a wide range of such chemicals, for example, chlorobenzenes, organosulfurs, organophosphates, and nitroaromatics. These chemicals are present or used in synthesis of explosive materials, insecticides, pollutants, and chemical warfare agents [3–15]. Their increased consumption and improper disposal have become serious environmental risk. Some of them are penetrating into the ground water through soil, causing serious environmental and health problems [16].

Nitrophenols (NPs) are primarily concerned toxic pollutants by the United States Environmental Protection Agency

(USEPA) [17], as these compounds have been found in industrial and agricultural wastes. These are anthropogenic, noxious, inhibitory, and biorefractory organic compounds and are considered as hazardous substances [18]. Among these, 2,4-dinitrophenol (2,4-DNP), 2,5-dinitrophenol (2,5-DNP), 2,6-trinitrophenol (2,6-DNP), and 2,4,6-TNP (2,4,6-TNP) are the most common and multipurpose industrial chemicals with wide-ranging applications as insecticides, dyes, drugs, and ordnance compounds [19–25]. Due to biorefractory properties of these pollutants, the biological techniques appear futile or take protracted incubation time on the degradation [26–28]. Thus, it is significantly important to develop new remediation methods for the decomposition of these organic pollutants.

Magnesium oxide nanoparticles were found as an effective adsorbent for the 2,4-dinitrotoluene (2,4-DNT) and 2,4,6-trinitrotoluene (2,4,6-TNT) [29]. Photocatalytic degradation of nitrophenols and nitroamines was also observed on

titanium oxide [12, 30, 31], iron oxide [16], and gold loaded aluminium oxide [32]. Activity of calcium oxide nanoparticles was studied against the degradation of dimethyl methylphosphonate (DMMP) and it was found that these nanoparticles have the ability to degrade other warfare chemical agents [5, 33]. Degradation of such compounds was also observed when aluminium oxide nanoparticles were used [3, 6, 9, 32].

Surfactants play an important role in the preparation of metal oxide nanoparticles because of their influence on particle growth, coagulation, and flocculation. Under hydrothermal condition, smallest particle size was reported by using anionic surfactant (SDS) as compared to cationic surfactant (CTABr) and nonionic surfactant (PEG) [34, 35]. Several methods like anodization [36], wet oxidation [37], sol-gel [38], hydrothermal treatment [34], deposition precipitation [22, 32], and thermal vapor deposition [39] methods are being applied for the synthesis of nanoparticles.

In the current study, CaO and $\text{Al}_2\text{O}_3\cdot\text{CaO}$ nanocatalysts were synthesized using hydrothermal method by varying the concentration of sodium dodecyl sulphate (SDS), an anionic surfactant. The objective of this study is to assess the photodegradation of selected ordnance compound by CaO and $\text{Al}_2\text{O}_3\cdot\text{CaO}$ nanocatalysts. The ordnance compound of concern, 2,4,6-TNP (2,4,6-trinitrophenol or picric acid), was considered of priority for this study. The effects of temperature and surfactant were studied for the synthesis of nanocatalysts, and catalytic properties of nanocatalysts were assessed for degradation of 2,4,6-TNP.

2. Materials and Methods

2.1. Materials. Calcium chloride anhydrous (CaCl_2), sodium hydroxide (NaOH), and sodium dodecyl sulfate (SDS) were purchased from Merck while aluminium chloride ($\text{AlCl}_3\cdot 6\text{H}_2\text{O}$) and methanol (CH_3OH) were from Riedel-de Haën. For the catalytic reaction, 2,4,6-TNP was purchased from Riedel-de Haën. All chemicals were used as received, without any further purification.

2.2. Characterization. The CaO nanocatalysts obtained were subjected to thermogravimetric analysis (TGA) by using SDT Q600 TGA. Structural analysis of CaO and $\text{Al}_2\text{O}_3\cdot\text{CaO}$ nanocatalysts was done using Fourier Transform Infrared (FTIR)—MIDAC 2000 with KBr powder and powder X-ray diffractometer (XRD) using PANalytical MPD X'PERT PRO. The diffraction patterns were compared using the standard database from International Centre for Diffraction Data (ICDD). The morphology and particle size of nanocatalysts was determined by FEI quanta 200 F Field Emission Scanning Electron Microscope (FESEM) and Philips CM12, 80 kV, Transmission Electron Microscope (TEM). HPLC analysis was performed on Shimadzu model LC 20-AT instrument equipped with diode array detector (SPD-M20A, Shimadzu). Chromatographic separation was performed by using C-18 column (250×4.6 mm, $5 \mu\text{m}$ packing) with isocratic solution. An injection volume of $20 \mu\text{L}$ was used for each sample. The peaks were observed at wavelength of 355 nm. GC-MS analyses were performed on Shimadzu model QP-2010 instrument.

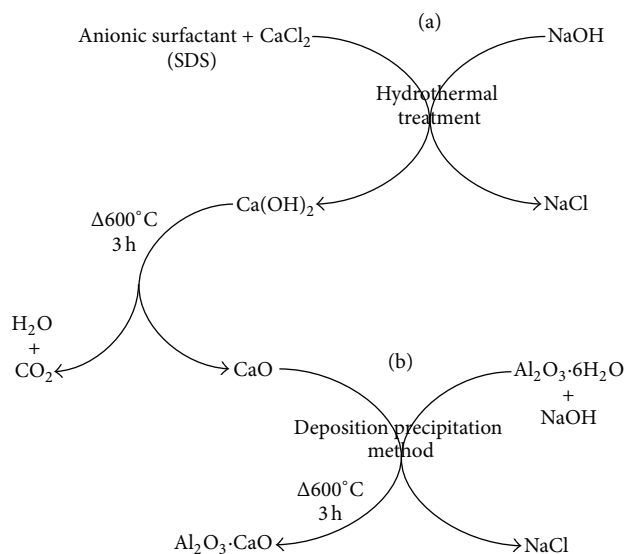


FIGURE 1: Experimental scheme for the synthesis of (a) CaO and (b) $\text{Al}_2\text{O}_3\cdot\text{CaO}$ nanocatalysts.

2.3. Synthesis of CaO Nanocatalysts by Hydrothermal Method. CaO nanocatalysts were synthesized by changing the experimental parameters, that is, temperature and concentration of surfactant, to study their effect on particle size and catalytic activity. Synthesis method of CaO is depicted in Figure 1(a).

The mixture containing 0.15 M of CaCl_2 and 0.008 M sodium dodecyl sulfate (SDS) was magnetically stirred at ambient temperature. The precursor to surfactant molar ratio was taken as 1 M : 0.05 M. Sodium hydroxide (0.30 M) solution was added dropwise and the reaction solution was stirred for 30 minutes. After stirring, the reaction suspension was placed in a Teflon line autoclave (hydrothermal bomb) and kept in an oven for 4 h at the desired temperatures (250, 180, 160, and 140°C).

After 4 h, the autoclave was removed from the oven and allowed to cool for 2 h at ambient temperature. The precipitates of Ca(OH)_2 were separated and washed 3 times with methanol and 2 times with deionized water to remove any reactant, ions, or surfactant and neutralize their pH by using centrifugation machine at the speed of 13000 rpm. The precipitates were dried and calcined at 600°C in a furnace with air flow for 3 h [40].

Similar process (Figure 1(a)) was adopted to study the effect of surfactant on CaO nanocatalysts. Only the molar concentration of SDS (0.004, 0.006, 0.008, 0.01, and 0.012 M) was varied to be close—and far from its critical micelle concentration (CMC) value which is 8.1 mM [41].

2.4. Preparation of Alumina Supported CaO Nanocatalysts by Deposition Precipitation Method. Synthesis of alumina doped CaO nanocatalysts was carried out by deposition precipitation method [32]. $\text{AlCl}_3\cdot 6\text{H}_2\text{O}$ and CaO nanocatalysts were used as precursors. 15 mM solution of $\text{AlCl}_3\cdot 6\text{H}_2\text{O}$ was prepared in 9 mL deionised water and 50 mg of CaO

nanocatalysts was added at different time intervals to attain pH 12.3 (isoelectric point) [42]. Meanwhile, the reaction was constantly stirred on magnetic stirring plate. Teflon line autoclave was filled with reaction solution and kept in the oven for 4 h at the same temperature as that of CaO nanocatalysts precursor. Similarly, the precipitates were washed and calcined. The experimental setup is displayed in Figure 1(b).

3. Results and Discussion

3.1. Thermogravimetric Analyses. Figure 2 shows TGA/DSC profile of the $\text{Ca}(\text{OH})_2$ synthesized with SDS at 180°C for 4 h via hydrothermal treatment. A significant weight loss (16.25%) is observed in the temperature range $375\text{--}450^\circ\text{C}$, which can be attributed to the thermal decomposition of $\text{Ca}(\text{OH})_2$. The observed weight loss in the range is smaller than the theoretical value (24.3%) calculated on the assumption of total dehydration of $\text{Ca}(\text{OH})_2$ to CaO [40].

The results indicate that a nearly complete conversion of $\text{Ca}(\text{OH})_2$ to CaO took place below 600°C . This implies that the surfactant used in the fabrication of CaO nanocatalysts had been almost removed at around 450°C .

3.2. Fourier Transform Infrared Analyses. FTIR peaks (Figure 3) at 3427 cm^{-1} and 3453 cm^{-1} can be attributed to the stretching and bending vibrations of hydrogen-bonded surface OH groups (physisorbed water). It reveals that only a slight amount of water molecules is retained in the fabricated CaO and $\text{Al}_2\text{O}_3\cdot\text{CaO}$ samples. The appearance of strong IR absorption band at 424 cm^{-1} may be attributed to the lattice vibrations of CaO [43]. The IR absorption bands at 1415 cm^{-1} and 1439 cm^{-1} are due to the symmetric stretching vibration of unidentate carbonate. Weak absorption band at 875 cm^{-1} further demonstrates the presence of carbonate species. This is due to exposure of highly reactive surface area of CaO to air during calcination which resulted in the formation of considerable amount of CO_2 and H_2O , which are adsorbed on the surface of CaO in the form of free $-\text{OH}$ and carbonate species. This indicates that surface $-\text{OH}$ and lattice oxygen of CaO do provide oxygen which is more assessable on high surface area samples (Figure 3(a)) [44, 45]. In Figure 3(b), the peaks at 821 cm^{-1} , 722 cm^{-1} , and 569 cm^{-1} are due to the stretching vibration of Al-O bond [46].

3.3. X-Ray Diffraction Analyses. The XRD pattern (Figure 4) of the CaO obtained with SDS heated at 180°C for 4 h after hydrothermal treatment shows that the nanocatalysts can be indexed to cubic CaO. Their lattice parameters agree well with the corresponding standard values given in JCPDS PDF# 82-1690 (CaO). The intense peaks at 32.2° , 37.3° , 54.5° , 64.5° , and 67.3° correspond to the (111), (200), (202), (311), and (222) crystal planes, respectively. The average crystallite size (3.15 nm) was determined from the broadenings of corresponding peaks by using Scherrer's equation:

$$D = \frac{k\lambda}{\beta(\cos\theta)}, \quad (1)$$

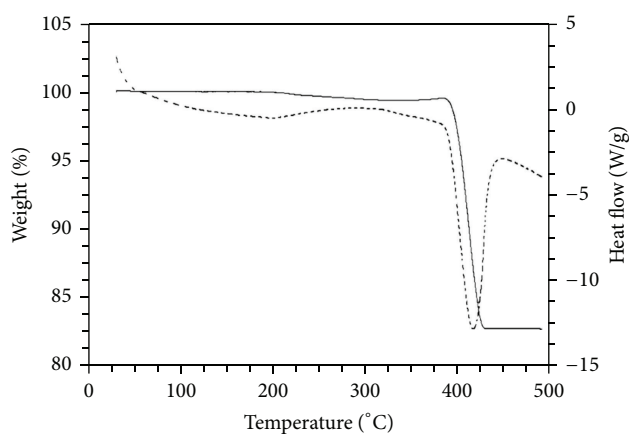


FIGURE 2: TGA (solid line)/DSC (dotted line) plots of uncalcined sample prepared with 0.008 M SDS at 180°C for 4 h.

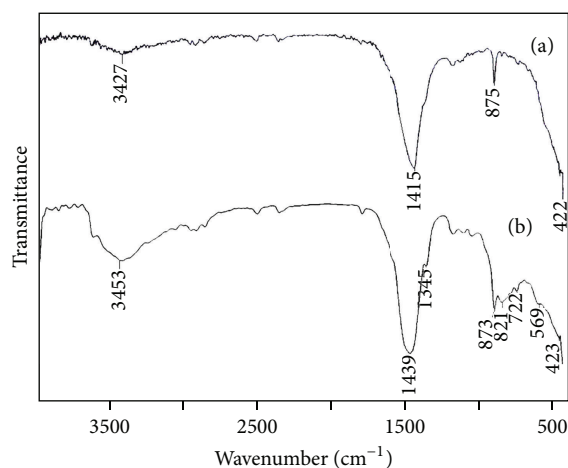


FIGURE 3: FTIR spectra for (a) CaO fabricated with surfactant (SDS) and (b) $\text{Al}_2\text{O}_3\cdot\text{CaO}$ nanocatalysts.

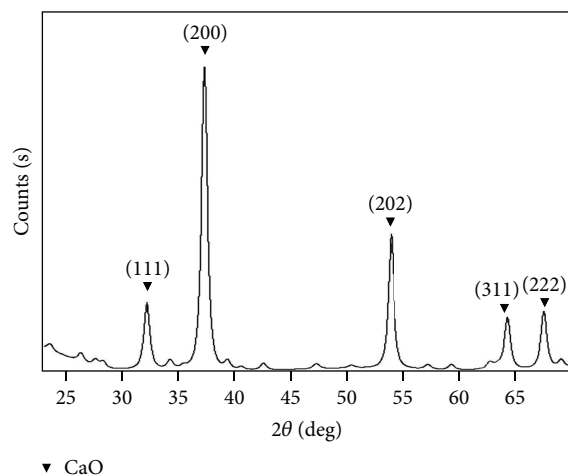


FIGURE 4: XRD pattern of CaO nanocatalyst fabricated with surfactant.

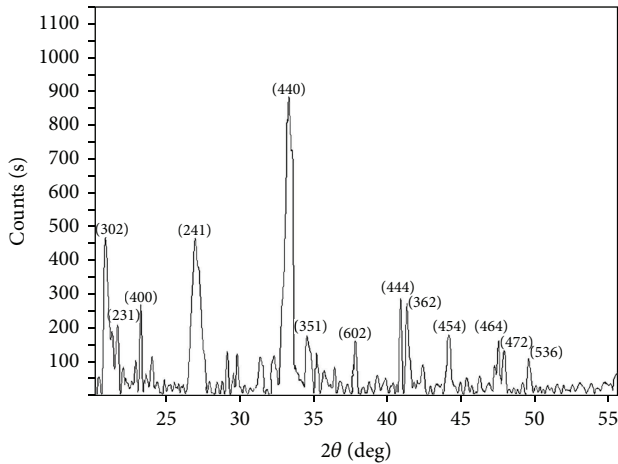


FIGURE 5: XRD pattern of $\text{Al}_2\text{O}_3\cdot\text{CaO}$ nanocatalyst.

where D is the mean crystallite size, k is the grain shape dependent constant 0.89, λ is the wavelength of the incident beam in nm, θ is the Bragg reflection angle, and β is the line broadening at half the maximum intensity in radians.

The 2θ values of $\text{Al}_2\text{O}_3\cdot\text{CaO}$ nanocatalysts (Figure 5) were compared with the ICDD database to identify the phase purity and composition formed. Aluminium forms $\text{Ca}_3\text{Al}_2\text{O}_6$ phase (PDF# 00-006-0495,) with the calcium oxide nanoparticles at 600°C due to strong Al–O interaction [47, 48]. The essential peaks at $2\theta = 20.9^\circ, 21.8^\circ, 23.3^\circ, 26.7^\circ, 33.2^\circ, 34.8^\circ, 37.2^\circ, 40.8^\circ, 41.4^\circ, 44.8^\circ, 48.8^\circ, 49.6^\circ,$ and 49.9° correspond to the lattice planes (302), (231), (400), (241), (440), (351), (602), (444), (362), (454), (464), (472), and (536), respectively. The average crystallite size of 3.64 nm for $\text{Ca}_3\text{Al}_2\text{O}_6$ was calculated by using (1). Uniform incorporation and distribution of aluminium into the CaO matrix may be responsible for the smaller crystallite size [49].

3.4. Optical Properties of $\text{Al}_2\text{O}_3\cdot\text{CaO}$ Nanocatalysts. Optical properties of $\text{Al}_2\text{O}_3\cdot\text{CaO}$ nanocatalysts were analyzed by UV-Vis absorption measurement at room temperature and using deionised water as blank. The sample was prepared by dispersing 3.6 mg of $\text{Al}_2\text{O}_3\cdot\text{CaO}$ nanocatalysts in 10 mL of deionised water and stirring by magnetic stirrer for 15 min. A homogeneous suspension solution was prepared and subjected for assessment for optical properties. Figure 6 describes typical absorption spectra of $\text{Al}_2\text{O}_3\cdot\text{CaO}$ nanocatalysts, which shows the shifting of absorption edges to the shorter wavelength (blue shift).

Equation (2) was used to calculate optical absorption coefficient α from absorption data:

$$\alpha = 2.303 \frac{10^3 \rho A}{lcM}, \quad (2)$$

where ρ is the theoretical density of $\text{Al}_2\text{O}_3\cdot\text{CaO}$ (3.03 g cm^{-3}), A is the absorbance of $\text{Al}_2\text{O}_3\cdot\text{CaO}$ nanocatalyst solution, l is the optical path length of quartz cell (1 cm), c is the molar

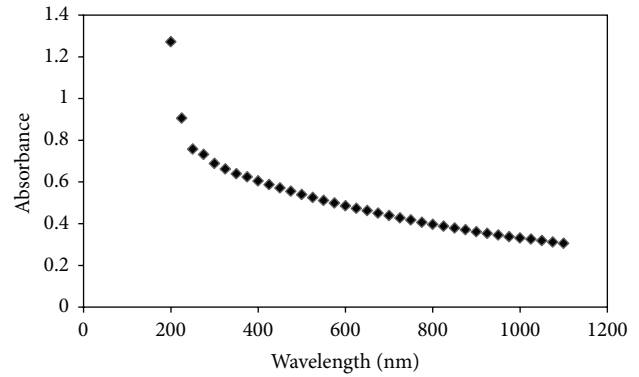


FIGURE 6: UV-Vis spectra for $\text{Al}_2\text{O}_3\cdot\text{CaO}$ nanocatalyst.

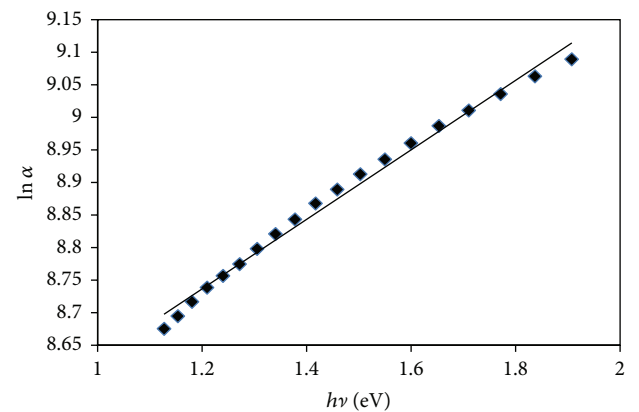


FIGURE 7: $\ln \alpha$ versus $h\nu$ for determination of the localized tail state E_e .

concentration of suspension solution, and M is the molecular weight of $\text{Al}_2\text{O}_3\cdot\text{CaO}$ nanocatalysts.

Using Urbach's equation (3), the density of the localized tail state ($E_e = 1.87 \text{ eV}$) in the forbidden energy gap was determined by plotting $\ln \alpha$ versus $h\nu$ as shown in Figure 7:

$$\alpha = \alpha_0 e^{h\nu/E_e}. \quad (3)$$

Here, α_0 is a constant and $h\nu$ is the energy of photons.

The optical band gap for direct transition was determined by plotting $(\alpha h\nu)^2$ versus $h\nu$ using

$$\alpha h\nu = B(h\nu - E_g)^n, \quad (4)$$

where B is constant and nature of transition n has been assumed to have values $1/2, 2, 3/2,$ and 3 for direct, indirect, forbidden direct, and forbidden indirect transitions, respectively [50, 51]. The direct optical band gap energy E_g is determined by extrapolating the linear portion of the curve in Figure 8; the intersection of the extrapolation gives the value of 3.3 eV, which is much less than band gap energy of Al_2O_3 (7.2 eV) [52].

Proposed behavior of $\text{Al}_2\text{O}_3\cdot\text{CaO}$ nanocatalyst towards organic pollutant due to band gap energy is illustrated in Figure 9.

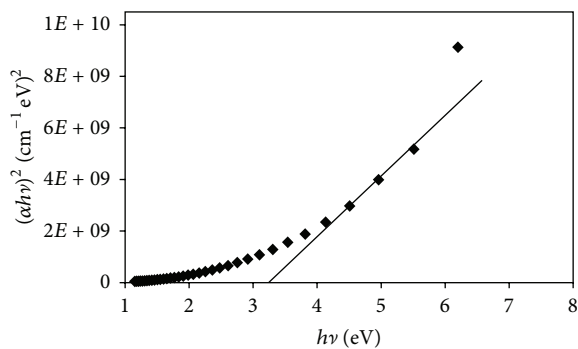


FIGURE 8: Plot of $(\alpha hv)^2$ versus $h\nu$ of $\text{Al}_2\text{O}_3\cdot\text{CaO}$ nanocatalysts.

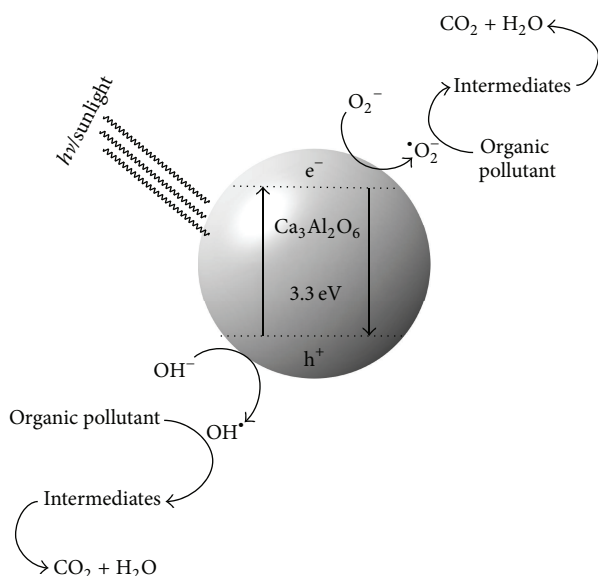


FIGURE 9: Mechanism of action of $\text{Al}_2\text{O}_3\cdot\text{CaO}$ nanocatalyst.

3.5. FESEM of CaO and $\text{Al}_2\text{O}_3\cdot\text{CaO}$ Nanocatalysts. Figures 10(a) and 10(b) provide the representative FESEM images of the CaO and $\text{Al}_2\text{O}_3\cdot\text{CaO}$ nanocatalysts fabricated with surfactant-assisted hydrothermal treatment at 180°C for 4 h and calcination at 600°C for 3 h. It was observed in Figure 10(a) that the CaO samples contain rounded coagulated nanocatalysts. After doping of alumina on CaO nanocatalysts, agglomerated particles of sample were observed in Figure 10(b).

3.6. TEM of CaO and $\text{Al}_2\text{O}_3\cdot\text{CaO}$ Nanocatalysts. Representative TEM image of the CaO and $\text{Al}_2\text{O}_3\cdot\text{CaO}$ nanocatalysts obtained after hydrothermal treatment is shown in Figure 11. The nanocatalysts exist in coagulated form with the particle size of 16 nm (Figure 11(a)). The particle size is decreased to 3.6 nm after the formation of $\text{Al}_2\text{O}_3\cdot\text{CaO}$ nanocatalysts (Figure 11(b)).

3.7. Catalytic Activity of CaO and $\text{Al}_2\text{O}_3\cdot\text{CaO}$ Nanocatalysts. A mixture of 5 mg of CaO nanocatalysts and 25 mL solution of 2,4,6-TNP (15 ppm) was placed under UV irradiation

with constant stirring for 15 minutes at ambient temperature. On the basis of Beer-Lambert law, calibration was done for 2,4,6-TNP at a wavelength of maximum absorptivity, λ_{max} , 356 nm [53]. The catalytic activity was determined using UV Spectrophotometer (UV-1700 Shimadzu) by measuring the change in absorbance at 356 nm every 60-second interval. Same procedure was adopted to determine catalytic activity of $\text{Al}_2\text{O}_3\cdot\text{CaO}$ nanocatalysts against 2,4,6-TNP [54]. The analysis of samples showed a continuous decrease in absorption at $\lambda_{\text{max}} = 356$ nm, which was used to track the degradation of 2,4,6-TNP [55]. It is evident that reaction kinetics of both CaO (Figure 12(a)) and $\text{Al}_2\text{O}_3\cdot\text{CaO}$ (Figure 12(b)) nanocatalysts with 2,4,6-TNP follows first order. The first order rate constant values, k' , were determined from the slope of the graphs as shown in Figures 12(a) and 12(b).

3.8. Effect of Variation of Temperature on Catalytic Activity of CaO Nanocatalysts. Catalytic activity of CaO nanocatalysts synthesized by varying hydrothermal treatment temperature (140, 160, 180, and 250°C) was studied while keeping other experimental parameters constant. It was observed that an increase in temperature (from 140°C to 180°C) resulted in increases in rate constant, k value (0.0732, 0.0791, and 0.1283 min^{-1}), but the catalytic activity decreases to 0.1124 min^{-1} at 250°C . This change in the catalytic activity trend suggests that high hydrothermal temperature favors fast reaction which increases the particle size and decreases the surface area and contributes to destructive adsorbent ability.

3.9. Effect of Variation of Surfactant Concentration on Catalytic Activity of CaO and $\text{Al}_2\text{O}_3\cdot\text{CaO}$ Nanocatalysts. The synthesis of CaO nanocatalysts under basic conditions is believed to follow the $X^- I^+ S^-$ module, where S^- is the anionic surfactant, I^+ is the inorganic precursor, and X^- is the counter ion [56]. A generalized mechanism of electrostatic interaction between inorganic precursor, surfactant and counter ions was proposed in Figure 13. When sodium hydroxide is added to the system, Na^+ and OH^- ions are supposed to surround $\text{Ca}^{2+}-\text{DS}^-$. The electrostatic attraction between Ca^{2+} and DS^- is stronger than that between Na and SD^- ions; this behavior enhances the particle formation [57]. Na^+ joins with Cl^- to make NaCl in the mixture system due to the electrostatic repulsion of Cl^- and DS^- . The OH^- ions self-assembled around the micelle, so Ca^{2+} ions were attracted towards OH^- to form $\text{Ca}(\text{OH})_2$ in the presence of surfactant (templating agent). In the final step of the process, the template was removed by calcination at 600°C for 3 h to generate pores.

The catalytic activity of CaO and $\text{Al}_2\text{O}_3\cdot\text{CaO}$ nanocatalysts (synthesized via hydrothermal treatment at 180°C and 4 h using different surfactant (SDS)) concentration is shown in Tables 1 and 2. It was observed that $\text{Al}_2\text{O}_3\cdot\text{CaO}$ nanocatalysts are more effective catalyst for the degradation of 2,4,6-TNP as compared to the CaO nanocatalysts. The rate constant values, k , of different samples of CaO and $\text{Al}_2\text{O}_3\cdot\text{CaO}$ nanocatalyst at the same parameters were compared. $\text{Al}_2\text{O}_3\cdot\text{CaO}$ nanocatalysts have higher rate constant (0.1251 min^{-1}) than CaO nanocatalyst (0.1233 min^{-1}) at 0.004 M concentration of SDS.

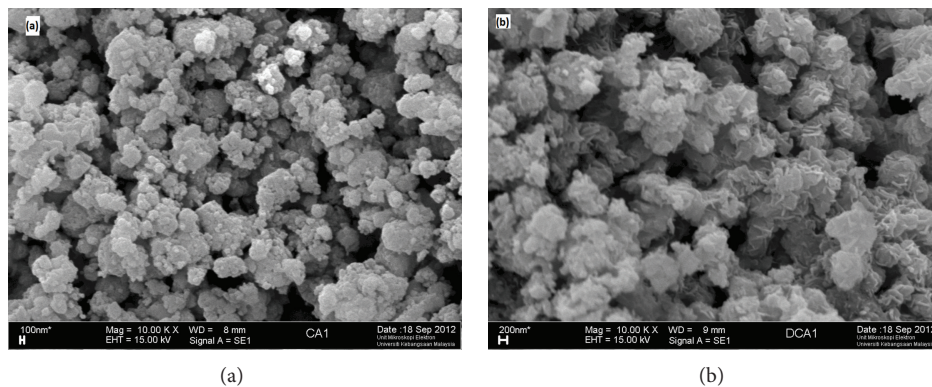


FIGURE 10: FESEM images for (a) CaO nanocatalysts fabricated with surfactant and (b) alumina supported CaO nanocatalysts.

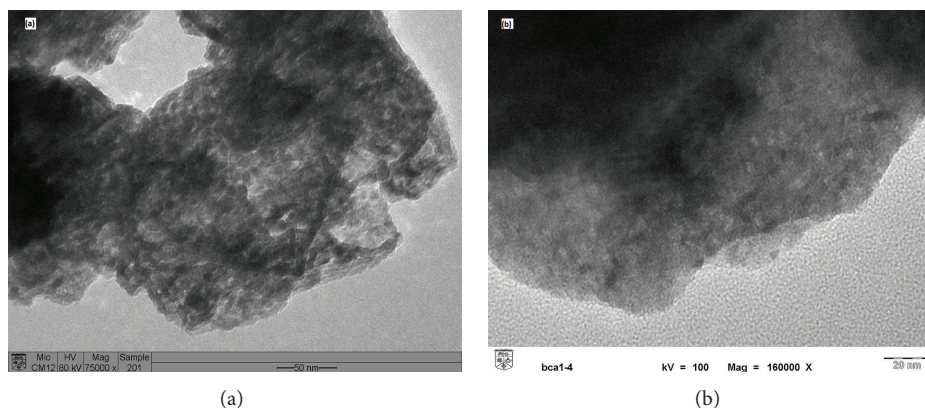


FIGURE 11: TEM images of (a) CaO and (b) $\text{Al}_2\text{O}_3\text{-CaO}$ nanocatalysts fabricated with surfactant (SDS).

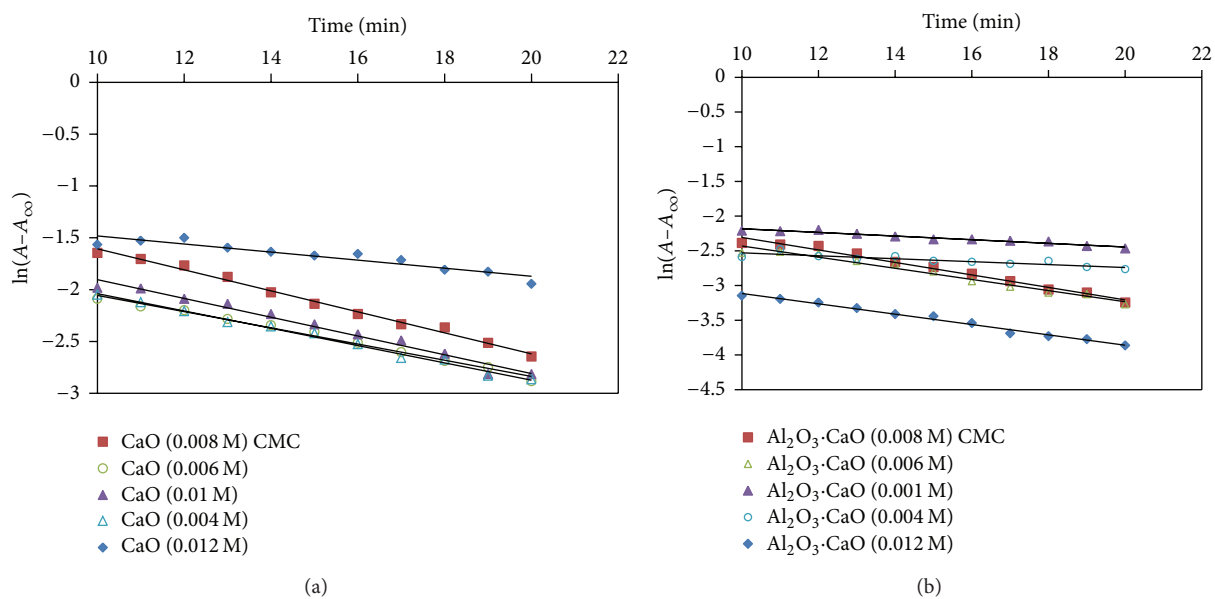


FIGURE 12: Plot of $\ln(A-A_{\infty})$ versus time for the oxidation of 2,4,6-TNP with (a) CaO and (b) $\text{Al}_2\text{O}_3\text{-CaO}$ nanocatalysts prepared under different concentrations of surfactant.

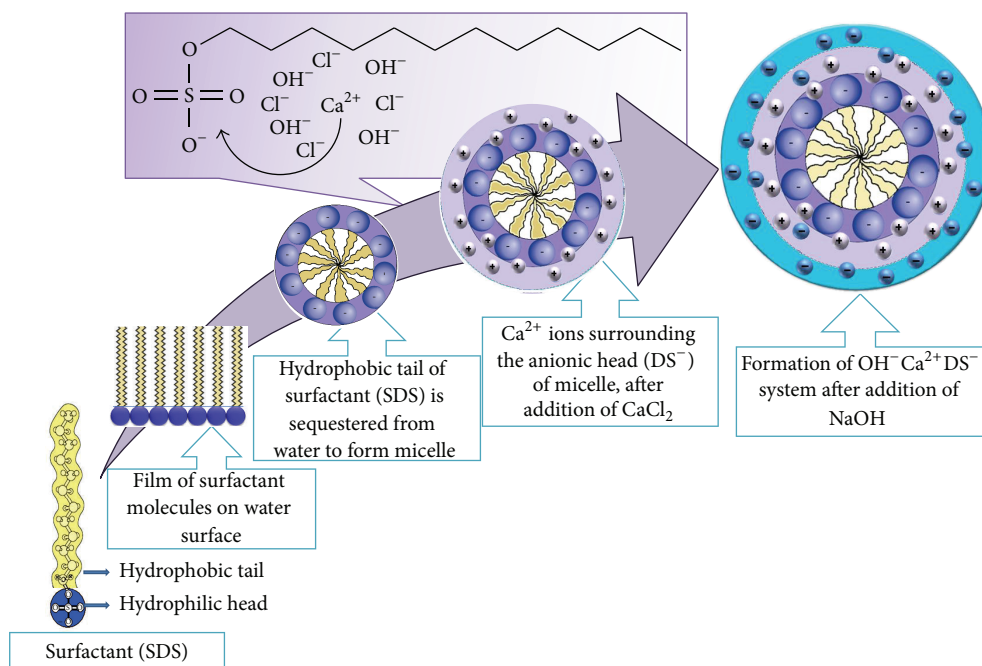


FIGURE 13: Mechanism of micelle assisted formation of OH^- - Ca^{2+} - DS^- system.

It was observed that the highest k values for both CaO and $\text{Al}_2\text{O}_3\cdot\text{CaO}$ were found at CMC of SDS in accordance to the small particle size of these nanocatalysts at this concentration. The k value increases (particle size decreases) when the nanocatalysts were prepared by using surfactant from 0.004 to 0.008 M as the precursors are well dispersed in the surfactant template. However, further increase in surfactant concentration from 0.008 to 0.012 M decreases the k values and increases the particle size due to formation of micelle which coagulates the particles. A parabola is formed showing the relationship between k values and surfactant concentration as shown in Figure 14.

3.10. Degradation Mechanism of 2,4,6-TNP. Degradation of 2,4,6-TNP by nanocatalysts was observed by HPLC and GC-MS analysis. A 15 ppm solution of picric acid (0.15 mg) was freshly prepared in 100 mL deionized water and used as standard solution. Mixtures of each (5 mg) calcium oxide and $\text{Al}_2\text{O}_3\cdot\text{CaO}$ nanocatalysts were prepared in 25 mL solution of 2,4,6-TNP (15 ppm) and placed under UV irradiation with constant stirring for 15 minutes at ambient temperature. The sample solutions were filtered and then degassed by sonication before use.

Mobile phase was prepared for HPLC analyses by mixing 70% methanol with 0.1M acetic acid buffer in the ratio of 97:3, v/v. The mobile phase was filtered and then degassed by sonication before use [58]. The data was analyzed by obtaining area under sample peaks at 355 nm. The observed retention time for standard 2,4,6-TNP solution was found 7.425 min as shown in Figure 15.

Each sample solution was injected separately in the HPLC and none of them showed any peak at the wavelength of

TABLE 1: Effect of surfactant concentration on catalytic activity of CaO nanocatalysts prepared at 180°C hydrothermal condition.

As-synthesized sample	Surfactant conc. (M)	"k" value (min^{-1})
CaO	0.004	0.1233
CaO	0.006	0.1243
CaO	0.008	0.1283
CaO	0.01	0.0931
CaO	0.012	0.0907

TABLE 2: Effect of surfactant concentration on catalytic activity of $\text{Al}_2\text{O}_3\cdot\text{CaO}$ nanocatalysts prepared at 180°C under hydrothermal condition.

As-synthesized sample	Surfactant conc. (M)	"k" value (min^{-1})
$\text{Al}_2\text{O}_3\cdot\text{CaO}$	0.004	0.1251
$\text{Al}_2\text{O}_3\cdot\text{CaO}$	0.006	0.1305
$\text{Al}_2\text{O}_3\cdot\text{CaO}$	0.008	0.1577
$\text{Al}_2\text{O}_3\cdot\text{CaO}$	0.01	0.0897
$\text{Al}_2\text{O}_3\cdot\text{CaO}$	0.012	0.0824

355 nm. These results lead to the conclusion that the picric acid was completely degraded by CaO and $\text{Al}_2\text{O}_3\cdot\text{CaO}$ nanocatalysts (Figure 16).

GC-MS technique was used to determine the intermediates generated during catalytic degradation of 2,4,6-TNP. Sample was prepared by suspending 5 mg $\text{Al}_2\text{O}_3\cdot\text{CaO}$ nanocatalysts in 25 mL solution of 2,4,6-TNP (15 ppm). Then, it was placed under UV irradiation with constant stirring for

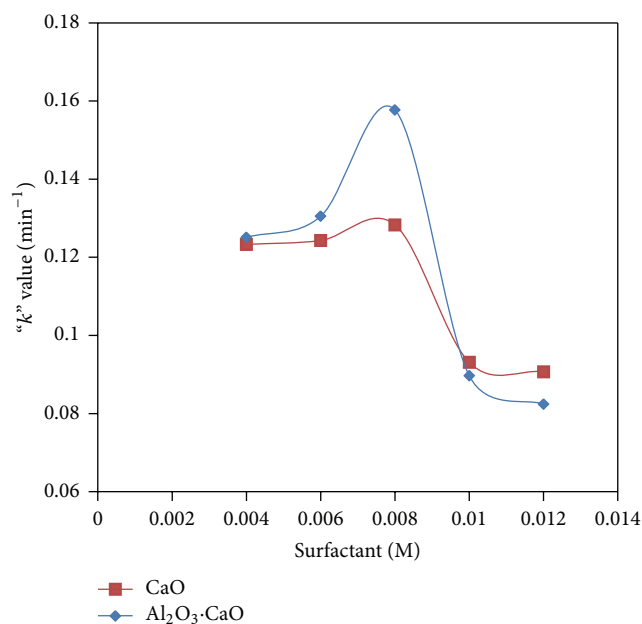


FIGURE 14: Plot of surfactant concentration versus rate constant “ k ” of the degradation of 2,4,6-TNP.

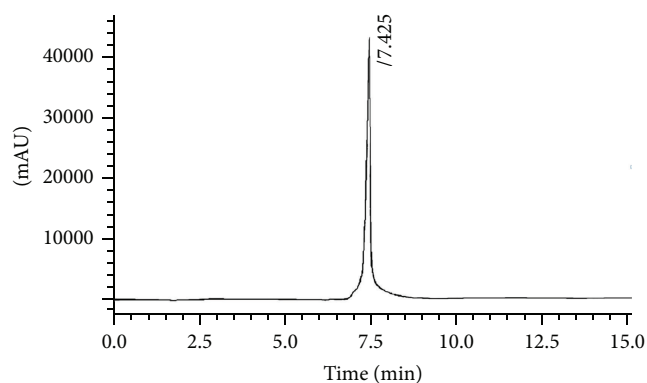


FIGURE 15: HPLC chromatogram for 2,4,6-TNP.

15 minutes at ambient temperature. The sample solution was filtered before use.

A schematic diagram is proposed as given in Scheme 1 on the basis of GC-MS chromatogram (Figure 17).

4. Conclusion

CaO and $\text{Al}_2\text{O}_3\cdot\text{CaO}$ nanocatalysts were prepared by varying the temperature and surfactant (SDS) concentration above and below CMC value using hydrothermal and using deposition precipitation method. Catalytic activity of these nanocatalysts was measured against the degradation of 2,4,6-TNP, which proved that the nanocatalysts are effective catalysts. The highest rate constant value, k , was observed in those samples which were prepared at CMC value of the

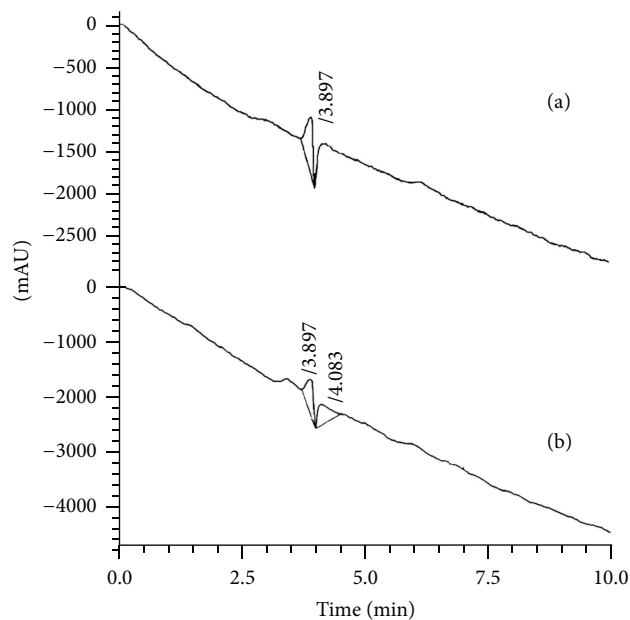


FIGURE 16: HPLC chromatograph showing the degradation of 2,4,6-TNP.

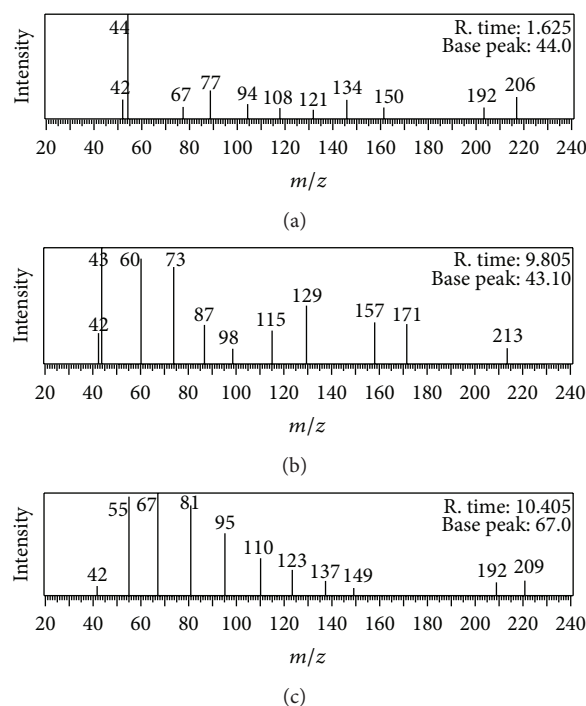
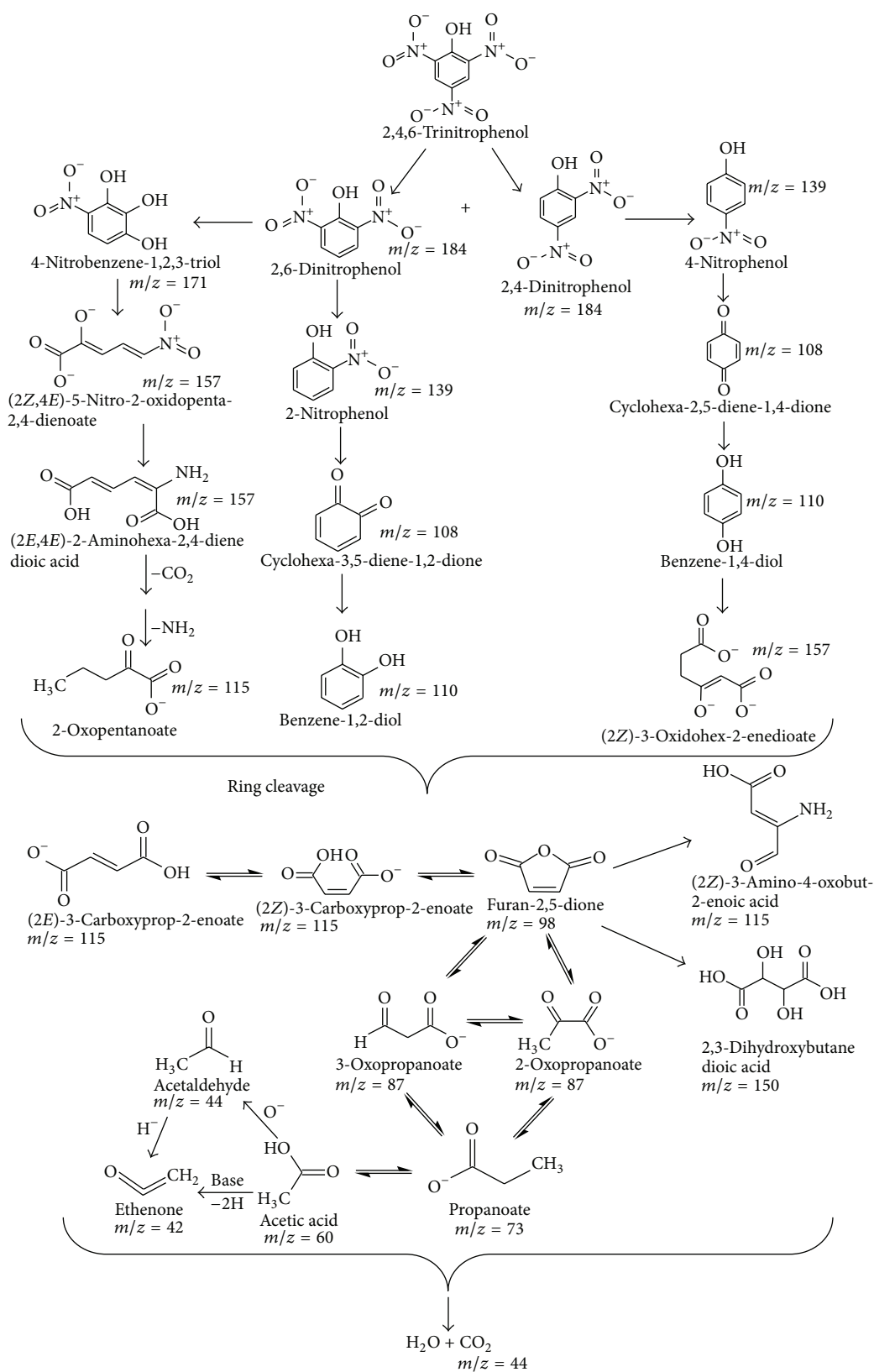


FIGURE 17: GC-MS chromatograms for degradation of 2,4,6-TNP by $\text{Al}_2\text{O}_3\cdot\text{CaO}$ nanocatalyst at retention time (a) 1.65 min, (b) 9.805 min, and (c) 10.405 min.

anionic surfactant. Compared to CaO nanocatalysts, the $\text{Al}_2\text{O}_3\cdot\text{CaO}$ nanocatalysts have the highest catalytic activity (0.1577 min^{-1}). The band gap of the $\text{Al}_2\text{O}_3\cdot\text{CaO}$ nanocatalyst was calculated as 3.3 eV.

SCHEME 1: Mechanism for degradation of 2,4,6-TNP by $\text{Al}_2\text{O}_3\text{-CaO}$ nanocatalyst.

Acknowledgments

XRD facilities provided by the Physics Department of GC University Lahore are gratefully acknowledged. The authors are grateful to The World Academy of Sciences (TWAS) for financial support to purchase scientific equipments to carry out this project and Universiti Sains Malaysia is acknowledged to provide characterization of samples by TEM through Research University (RU) Grant no. 1001/PKIMIA/815099.

References

- [1] M. A. Henderson, T. Jin, and J. M. White, "The desorption and decomposition of trinitrotoluene adsorbed on metal oxide powders," *Applied Surface Science*, vol. 27, no. 1, pp. 127–140, 1986.
- [2] K. J. Klabunde and R. Richards, *Nanoscale Materials in Chemistry*, John Wiley & Sons, 2009.
- [3] T. Z. Tzou and S. W. Weller, "Catalytic oxidation of dimethyl methylphosphonate," *Journal of Catalysis*, vol. 146, no. 2, pp. 370–374, 1994.
- [4] G. W. Wagner, P. W. Bartram, O. Koper, and K. J. Klabunde, "Reactions of VX, GD, and HD with nanosize MgO," *The Journal of Physical Chemistry B*, vol. 103, no. 16, pp. 3225–3228, 1999.
- [5] G. W. Wagner, O. B. Koper, E. Lucas, S. Decker, and K. J. Klabunde, "Reactions of VX, GD, and HD with nanosize CaO: autocatalytic dehydrohalogenation of HD," *The Journal of Physical Chemistry B*, vol. 104, no. 21, pp. 5118–5123, 2000.
- [6] G. W. Wagner, L. R. Procell, R. J. O'Connor et al., "Reactions of VX, GB, GD, and HD with nanosize Al_2O_3 . Formation of aluminophosphonates," *Journal of the American Chemical Society*, vol. 123, no. 8, pp. 1636–1644, 2001.
- [7] S. M. Kanan, Z. Lu, and C. P. Tripp, "A comparative study of the adsorption of chloro- and non-chloro-containing organophosphorus compounds on WO_3 ," *The Journal of Physical Chemistry B*, vol. 106, no. 37, pp. 9576–9580, 2002.
- [8] X. Ma, M. Zheng, W. Liu, Y. Qian, B. Zhang, and W. Liu, "Dechlorination of hexachlorobenzene using ultrafine Ca–Fe composite oxides," *Journal of Hazardous Materials*, vol. 127, no. 1–3, pp. 156–162, 2005.
- [9] J. C. Chen and C. T. Tang, "Preparation and application of granular ZnO/ Al_2O_3 catalyst for the removal of hazardous trichloroethylene," *Journal of Hazardous Materials*, vol. 142, no. 1–2, pp. 88–96, 2007.
- [10] W. O. Gordon, B. M. Tissue, and J. R. Morris, "Adsorption and decomposition of dimethyl methylphosphonate on Y_2O_3 nanoparticles," *The Journal of Physical Chemistry C*, vol. 111, no. 8, pp. 3233–3240, 2007.
- [11] O. B. Koper, S. Rajagopalan, S. Winecki, and K. J. Klabunde, "Nanoparticle metal oxides for chlorocarbon and organophosphonate remediation," in *Environmental Applications of Nanomaterials: Synthesis, Sorbents and Sensors*, pp. 3–24, 2007.
- [12] D. Crokek, P. A. Kemme, O. V. Makarova, L. X. Chen, and T. Rajh, "Selective photocatalytic decomposition of nitrobenzene using surface modified TiO_2 nanoparticles," *The Journal of Physical Chemistry C*, vol. 112, no. 22, pp. 8311–8318, 2008.
- [13] G. W. Wagner, Q. Chen, and Y. Wu, "Reactions of VX, GD, and HD with nanotubular titania," *The Journal of Physical Chemistry C*, vol. 112, no. 31, pp. 11901–11906, 2008.
- [14] A. Saxena, H. Mangal, P. K. Rai, A. S. Rawat, V. Kumar, and M. Datta, "Adsorption of diethylchlorophosphate on metal oxide nanoparticles under static conditions," *Journal of Hazardous Materials*, vol. 180, no. 1–3, pp. 566–576, 2010.
- [15] L. A. Patil, A. R. Bari, M. D. Shinde, V. Deo, and M. P. Kaushik, "Detection of dimethyl methyl phosphonate—a simulant of sarin: the highly toxic chemical warfare—using platinum activated nanocrystalline ZnO thick films," *Sensors and Actuators B*, vol. 161, no. 1, pp. 372–380, 2012.
- [16] A. Halasz, C. Groom, E. Zhou et al., "Detection of explosives and their degradation products in soil environments," *Journal of Chromatography A*, vol. 963, no. 1–2, pp. 411–418, 2002.
- [17] USEPA, *Health and Environmental Effects Profile for Nitrophenols*, Environmental Protection Agency, Environmental Criteria and Assessment Office, Cincinnati, Ohio, USA, 1985.
- [18] R. Belloli, E. Bolzacchini, L. Clerici, B. Rindone, G. Sesana, and V. Librando, "Nitrophenols in air and rainwater," *Environmental Engineering Science*, vol. 23, no. 2, pp. 405–415, 2006.
- [19] M. Shimazu, A. Mulchandani, and W. Chen, "Simultaneous degradation of organophosphorus pesticides and p-nitrophenol by a genetically engineered *Moraxella* sp. with surface-expressed organophosphorus hydrolase," *Biotechnology and Bioengineering*, vol. 76, no. 4, pp. 318–324, 2001.
- [20] J. B. Lippincot, *List of Worldwide Hazardous Chemical and Pollutants*, The Forum for Scientific Excellence, New York, NY, USA, 1990.
- [21] M. S. Dieckmann and K. A. Gray, "A comparison of the degradation of 4-nitrophenol via direct and sensitized photocatalysis in TiO_2 slurries," *Water Research*, vol. 30, no. 5, pp. 1169–1183, 1996.
- [22] S. Ali, M. A. Farrukh, and M. Khaleeq-ur-Rahman, "Photodegradation of 2,4,6-trinitrophenol catalyzed by Zn/MgO nanoparticles prepared under aqueous-organic medium," *Korean Journal of Chemical Engineering*, vol. 30, no. 11, 2013.
- [23] A. Gutes, F. Céspedes, S. Alegret, and M. del Valle, "Determination of phenolic compounds by a polyphenol oxidase amperometric biosensor and artificial neural network analysis," *Biosensors and Bioelectronics*, vol. 20, no. 8, pp. 1668–1673, 2005.
- [24] K. Tanaka, K. Padermpole, and T. Hisanaga, "Photocatalytic degradation of commercial azo dyes," *Water Research*, vol. 34, no. 1, pp. 327–333, 2000.
- [25] K. W. Hofmann, H.-J. Knackmuss, and G. Heiss, "Nitrite elimination and hydrolytic ring cleavage in 2,4,6-trinitrophenol (picric acid) degradation," *Applied and Environmental Microbiology*, vol. 70, no. 5, pp. 2854–2860, 2004.
- [26] Z. Aleksieva, D. Ivanova, T. Godjevargova, and B. Atanasov, "Degradation of some phenol derivatives by *Trichosporon cutaneum* R57," *Process Biochemistry*, vol. 37, no. 11, pp. 1215–1219, 2002.
- [27] S. Yi, W.-Q. Zhuang, B. Wu, S. T.-L. Tay, and J.-H. Tay, "Biodegradation of p-nitrophenol by aerobic granules in a sequencing batch reactor," *Environmental Science and Technology*, vol. 40, no. 7, pp. 2396–2401, 2006.
- [28] M. C. Tomei, M. C. Annesini, R. Luberti, G. Cento, and A. Senia, "Kinetics of 4-nitrophenol biodegradation in a sequencing batch reactor," *Water Research*, vol. 37, no. 16, pp. 3803–3814, 2003.
- [29] V. M. Boddu, D. S. Viswanath, and S. W. Maloney, "Synthesis and characterization of coralline magnesium oxide nanoparticles," *Journal of the American Ceramic Society*, vol. 91, no. 5, pp. 1718–1720, 2008.
- [30] Y. Liu, H. Liu, J. Ma, and X. Wang, "Comparison of degradation mechanism of electrochemical oxidation of di- and

- tri-nitrophenols on Bi-doped lead dioxide electrode effect of the molecular structure," *Applied Catalysis B*, vol. 91, no. 1-2, pp. 284-299, 2009.
- [31] O. V. Makarova, T. Rajh, M. C. Thurnauer, A. Martin, P. A. Kempe, and D. Crokek, "Surface modification of TiO₂ nanoparticles for photochemical reduction of nitrobenzene," *Environmental Science and Technology*, vol. 34, no. 22, pp. 4797-4803, 2000.
- [32] H. Yazid, R. Adnan, and M. A. Farrukh, "Gold nanoparticles supported on titania for the reduction of p-nitrophenol," *Indian Journal of Chemistry A*, vol. 52, no. 2, pp. 184-191, 2013.
- [33] Y. Paukku, A. Michalkova, and J. Leszczynski, "Adsorption of dimethyl methylphosphonate and trimethyl phosphite on calcium oxide: an ab initio study," *Structural Chemistry*, vol. 19, no. 2, pp. 307-320, 2008.
- [34] M. A. Farrukh, P. Tan, and R. Adnan, "Influence of reaction parameters on the synthesis of surfactant-assisted tin oxide nanoparticles," *Turkish Journal of Chemistry*, vol. 36, no. 2, pp. 303-314, 2012.
- [35] S. Gnanam and V. Rajendran, "Anionic, cationic and non-ionic surfactants-assisted hydrothermal synthesis of tin oxide nanoparticles and their photoluminescence property," *Digest Journal of Nanomaterials and Biostructures*, vol. 5, no. 3, pp. 623-628, 2010.
- [36] H.-S. Goh, R. Adnan, and M. A. Farrukh, "ZnO nanoflake arrays prepared via anodization and their performance in the photodegradation of methyl orange," *Turkish Journal of Chemistry*, vol. 35, no. 3, pp. 375-391, 2011.
- [37] K. M. A. Saron, M. R. Hashim, and M. A. Farrukh, "Stress control in ZnO films on GaN/Al₂O₃ via wet oxidation of Zn under various temperatures," *Applied Surface Science*, vol. 258, no. 13, pp. 5200-5205, 2012.
- [38] R. Adnan, N. A. Razana, I. A. Rahman, and M. A. Farrukh, "Synthesis and characterization of high surface area tin oxide nanoparticles via the sol-gel method as a catalyst for the hydrogenation of styrene," *Journal of the Chinese Chemical Society*, vol. 57, no. 2, pp. 222-229, 2010.
- [39] K. M. A. Saron, M. R. Hashim, and M. A. Farrukh, "Growth of GaN films on silicon (111) by thermal vapor deposition method: optical functions and MSM UV photodetector applications," *Superlattices and Microstructures*, vol. 64, pp. 88-97, 2013.
- [40] C. Liu, L. Zhang, J. Deng, Q. Mu, H. Dai, and H. He, "Surfactant-aided hydrothermal synthesis and carbon dioxide adsorption behavior of three-dimensionally mesoporous calcium oxide single-crystallites with tri-, tetra-, and hexagonal morphologies," *The Journal of Physical Chemistry C*, vol. 112, no. 49, pp. 19248-19256, 2008.
- [41] H. B. de Aguiar, M. L. Strader, A. G. F. de Beer, and S. Roke, "Surface structure of sodium dodecyl sulfate surfactant and oil at the oil-in-water droplet liquid/liquid interface: a manifestation of a nonequilibrium surface state," *The Journal of Physical Chemistry B*, vol. 115, no. 12, pp. 2970-2978, 2011.
- [42] D. A. Sverjensky, "Zero-point-of-charge prediction from crystal chemistry and solvation theory," *Geochimica et Cosmochimica Acta*, vol. 58, no. 14, pp. 3123-3129, 1994.
- [43] M. I. Zaki, H. Knözinger, B. Tesche, and G. A. H. Mekhemer, "Influence of phosphonation and phosphorylation on surface acid-base and morphological properties of CaO as investigated by *in situ* FTIR spectroscopy and electron microscopy," *Journal of Colloid and Interface Science*, vol. 303, no. 1, pp. 9-17, 2006.
- [44] O. B. Koper, I. Lagadic, A. Volodin, and K. J. Klabunde, "Alkaline-earth oxide nanoparticles obtained by aerogel methods. Characterization and rationale for unexpectedly high surface chemical reactivities," *Chemistry of Materials*, vol. 9, no. 11, pp. 2468-2480, 1997.
- [45] Y. X. Li, H. Li, and K. J. Klabunde, "Destructive adsorption of chlorinated benzenes on ultrafine (Nanoscale) particles of magnesium oxide and calcium oxide," *Environmental Science and Technology*, vol. 28, no. 7, pp. 1248-1253, 1994.
- [46] J. Hemalatha, T. Prabhakaran, and R. P. Nalini, "A comparative study on particle-fluid interactions in micro and nanofluids of aluminium oxide," *Microfluidics and Nanofluidics*, vol. 10, no. 2, pp. 263-270, 2011.
- [47] B. Viswanath and N. Ravishankar, "Interfacial reactions in hydroxyapatite/alumina nanocomposites," *Scripta Materialia*, vol. 55, no. 10, pp. 863-866, 2006.
- [48] J. Yu, Q. Ge, W. Fang, and H. Xu, "Influences of calcination temperature on the efficiency of CaO promotion over CaO modified Pt/ γ -Al₂O₃ catalyst," *Applied Catalysis A*, vol. 395, no. 1-2, pp. 114-119, 2011.
- [49] R. Koirala, G. K. Reddy, and P. G. Smirniotis, "Single nozzle flame-made highly durable metal doped Ca-based sorbents for CO₂ capture at high temperature," *Energy & Fuels*, vol. 26, no. 5, pp. 3103-3109, 2012.
- [50] A. Gaber, A. Y. Abdel-Latif, M. A. Abdel-Rahim, and M. N. Abdel-Salam, "Thermally induced structural changes and optical properties of tin dioxide nanoparticles synthesized by a conventional precipitation method," *Materials Science in Semiconductor Processing*, vol. 16, no. 6, pp. 1784-1790, 2013.
- [51] E. Filippo, D. Manno, A. R. de Bartolomeo, and A. Serra, "Single step synthesis of SnO₂-SiO₂ core-shell microcables," *Journal of Crystal Growth*, vol. 330, no. 1, pp. 22-29, 2011.
- [52] S. J. Mousavi, M. R. Abolhassani, S. M. Hosseini, and S. A. Sebt, "Comparison of electronic and optical properties of the and phases of alumina using density functional theory," *Chinese Journal of Physics*, vol. 47, no. 6, pp. 862-873, 2009.
- [53] V. Pimienta, R. Etchenique, and T. Buhse, "On the origin of electrochemical oscillations in the picric acid/CTAB two-phase system," *The Journal of Physical Chemistry A*, vol. 105, no. 44, pp. 10037-10044, 2001.
- [54] M. Ksibi, A. Zemzemi, and R. Boukchina, "Photocatalytic degradability of substituted phenols over UV irradiated TiO₂," *Journal of Photochemistry and Photobiology A*, vol. 159, no. 1, pp. 61-70, 2003.
- [55] J. Li, H. Qiao, Y. Du et al., "Electrospinning synthesis and photocatalytic activity of mesoporous TiO₂ nanofibers," *The Scientific World Journal*, vol. 2012, Article ID 154939, 7 pages, 2012.
- [56] M. A. Farrukh, B.-T. Heng, and R. Adnan, "Surfactant-controlled aqueous synthesis of SnO₂ nanoparticles via the hydrothermal and conventional heating methods," *Turkish Journal of Chemistry*, vol. 34, no. 4, pp. 537-550, 2010.
- [57] H. Iyota and R. Krastev, "Miscibility of sodium chloride and sodium dodecyl sulfate in the adsorbed film and aggregate," *Colloid and Polymer Science*, vol. 287, no. 4, pp. 425-433, 2009.
- [58] *NIOSH Manual of Analytical Methods*, vol. 4, method no. S228, US Department of Health and Human Services, Public Health Services, 2nd edition, 1978.



Hindawi

Submit your manuscripts at
<http://www.hindawi.com>

